TITLE: In situ characterization of nanoscale strains in loaded whole joints via synchrotron X-ray tomography

AUTHORS: Kamel Madi, Katherine A. Staines, Brian K. Bay, Behzad Javaheri, Hua Geng, Andrew J. Bodey, Sarah Cartmell, Andrew A. Pitsillides & Peter D. Lee

JOURNAL TITLE: Nature Biomedical Engineering

PUBLICATION DATE: 25 November 2019

PUBLISHER: Nature Publishing Group

DOI: 10.1038/s41551-019-0477-1

In situ characterization of nanoscale strains in loaded whole joints via synchrotron X-ray tomography

Madi K[1,2#], Staines KA[3#], Bay BK[4*], Javaheri B[5], Geng, H[1,6], Bodey AJ[7], Cartmell S[6], Pitsillides AA[5*], Lee PD[1,8*]

Joint first authorship: Madi, Staines, * Joint senior and corresponding authors: Lee, Pitsillides, Bay

[1] Research Complex at Harwell, RAL, Didcot, OX11 0FA, UK

[2] 3Dmagination Ltd, Fermi Avenue, Harwell Oxford, Didcot, OX11 0QR, UK

[3] School of Applied Sciences, Edinburgh Napier University, Edinburgh, EH11 4BN, UK

[4] College of Engineering, Oregon State University, Corvallis, OR, 97331, USA

[5] Comparative Biomedical Sciences, Royal Veterinary College, Royal College Street, London, NW10TU, UK

[6] Department of Materials, The University of Manchester, Manchester, M13 9PL, UK

[7] Diamond Light Source, Harwell Science & Innovation Campus, Oxfordshire, OX11 0DE, UK

[8] Mechanical Engineering, University College London, London, WC1E 7JE, UK

Abstract

Imaging techniques for quantifying how the hierarchical structure of deforming joints changes are constrained by destructive sample treatments, sample-size restrictions and lengthy scan times. Here, we report the use of fast, low-dose pink-beam synchrotron X-ray tomography combined with mechanical loading at nanometric precision for the *in situ* imaging, at resolutions lower than 100 nm, of mechanical strain in intact untreated joints under physiologically realistic conditions. We show that, in young, aged, and osteoarthritic mice, hierarchical changes in tissue structure and mechanical behaviour can be simultaneously visualized, and that tissue structure at the cellular level correlates with whole-joint mechanical performance. We also used the tomographic approach to study the co-localization of tissue strains to specific chondrocyte lacunar organizations within intact loaded joints, and for the exploration of the role of calcified-cartilage stiffness on the biomechanics of healthy and pathological joints.

One-sentence editorial summary:

Pink-beam synchrotron X-ray tomography combined with mechanical loading at nanometric precision enables the *in situ* imaging of intact untreated joints, resolving strains at sub-100-nm resolution.

Imaging methods have proven essential to our understanding a range of key biomechanical systems. This has been particularly true for musculoskeletal challenges, such as understanding a joint's mechanical function, healthy ageing and the impact of changes in articular cartilage integrity on locomotion. Safeguarding the avascular, aneural articular cartilage tissue places burden on neighbouring mineralised tissues. Extensive incidence of degeneration of the entire joint in osteoarthritis is *prima facie* evidence of the likely scale of this threat. However, current imaging techniques are unable to resolve this detail *in situ*. Further, joint mechanics are also believed to be dominated by the extracellular matrix of the hyaline cartilage and by mineralized subchondral regions, where cancellous bone capped by a cortical plate is found beneath calcified cartilage, which merges with hyaline cartilage. These tissues are known to retain distinct physiology, structure and mechanics, but how they interact at the nano-scale to secure healthy joint mechanics under physiologically representative loading remains undefined. A method for resolving the ultra-structure of the joint, and in particular, the management of tissue strain as joint compressive stresses are transmitted from the low stiffness articular cartilage through to the high stiffness cortical plate is required.

Current imaging methods of this key biomechanical system have advanced tremendously, but each is restricted to either scale or application. Nano-scale imaging in other contexts is now possible via many approaches[1-4]. For example small-angle and wide-angle X-ray scattering can yield bone collagen fibril/ mineral phase information as well as 3-dimensional (3D) strain maps; however, these nano-scale approaches can only measure thin tissue fragments[5-8], or average the strain through thickness. Most require a very high X-ray dose, causing damage and/or limiting the technique to hard tissue. Further, many techniques are only applicable on thin histological samples due to field of view limitations. This failure to retain organ-level integrity due to restrictions imposed by scan conditions also arises in ptychography and focused ion beam scanning and transmission electron microscopy (FIB-SEM/TEM)[9-12]. Confocal microscopic alternatives for nano-scale imaging require staining to achieve anisotropic spatial resolution but can be applied only to a very restricted tissue depth[13,14]. Optical/confocal microscopy with 2D/3D digital image correlation (DIC) is also hampered by tissue opacity, distorting and limiting the resolution and depth[15-19]. Indentation-atomic force microscopy delivers nanomechanics yet is restricted to surface imaging by inefficient 'deep' probing and tissue processing[20-22]. A method compatible with volumetric, ultra-high resolution imaging and quantification of mechanical strain during the repeated *in situ* biomechanical characterisation of hierarchical structure during loading of an intact sample, such as a whole joint, is therefore highly desirable.

Magnetic resonance does allow the probing of whole joints at macroscopic scales, but imposes limits both upon spatial and temporal resolution. On the other hand, X-ray computed tomography (CT) yields greater spatial resolution, is nominally non-destructive, attuned to repeat imaging and offers excellent field of view trade-offs which, together with digital volume correlation (DVC), can realise full-field continuum- and tissue-level strain measurement[23-26]. The greater flux and high-end instrumentation in synchrotron computed tomography (sCT) enables even higher spatial and temporal resolution, making it ideal for rapid collection of multiple 3D volumes during *in situ* loading. However, sCT may cause substantial tissue damage and thus beam configuration and scan parameters that maintain both tissue integrity and tomographic reconstruction quality are required to enable DVC accuracy. The resolving of *in situ* nano-scale strain in intact mineralized tissues has however been deemed unattainable[27]. Improved methodologies are required to: i) enhance resolution without compromising field of view; ii) lessen total radiation exposure to preserve tissue mechanics[28]; iii) curb sample motion during scanning, and; iv) control *in situ* load application to high levels of precision, in this case, to un-sectioned bones and intact joints. Additionally, significant advances are also required in

DVC algorithms, allowing variable density point clouds that match the complex shape and internal microstructure of the bones comprising the joint's structure that matches the imaging technique's resolution.

Herein, our sCT method attains greater resolution and imaging speed, allowing for DVC-based strain fields calculated from displacements with better than 100 nm accuracy within intact, untreated mechanically loaded mouse bones and knee joints in physiological orientation. To understand the biomechanical functionality of the joint in health and in osteoarthritis, we have applied our method to STR/Ort and CBA mouse joints. The STR/Ort mouse is a well-established, spontaneous model of osteoarthritis, with disease resembling that in humans. Mice develop articular cartilage lesions predominantly on the tibia plateau, with other expected degenerative changes coinciding with the attainment of sexual maturity[29]. CBA mice are the most appropriate control for the STR/Ort mouse as they are the nearest available parental strain, and extensive analysis reveals they show no overt signs of osteoarthritis with ageing[29]. We demonstrate how our methods pinpoint many hitherto unaddressed questions in joint mechanobiology, including the extent to which osteoarthritis-prone joints exhibit: (i) greater chondrocyte hypertrophy, (ii) abnormally high strains in the calcified cartilage, (iii) localised calcified cartilage cracking and (iv) development of tissue strains consistent with a stiffer articular construct. These quantitative imaging methods bridge gaps between whole joint mechanics and nanoscale strain development in sub-articular tissues, enabling the elusive structural cartilage-bone hierarchical features underpinning joint health and disease to be defined.

Results

Fast sCT imaging of nano-resolved load-induced strains in intact mouse joints: was enabled via satisfying the challenging trade-off between spatial resolution, field of view (FOV), signal to noise ratio (SNR), DVC accuracy, radiation dose, and sample motion. To achieve nano-resolution in intact joints, we employed high-flux/short-exposure continuous imaging to facilitate high efficacy collection of less damaging high-energy photons, reducing tissue exposure to ionizing radiation (Suppl. Methods). The high efficacy imaging was achieved using high and low bandpass filtering, tailored to select harmonics primary centred at 20 keV, producing a high-flux 'pink' beam[30] coupled to a high dynamic range pco.edge 5.5 sCMOS camera (Fig. 1A and Methods), allowing collection of 2401 projections with 30% transmission in 4.4 minutes (FOV 4.1x3.45 mm, effective pixel size 1.6 μm, 2401 projections, SNR ~1.4; see Setup 1 in Suppl. Table ST1).

Applying these conditions to entire knee joints enabled cell lacunae in the calcified cartilage (hypertrophic chondrocytes) and subchondral bone (osteocytes) to be readily resolved with unprecedented resolution for the radiation dose (~100 kGy; Fig. 1B-E) and speed (Suppl. Table ST1-Setup 1 and Suppl. Fig. S3c,f). This compares to the equivalent monochromatic beam setup dose of ~157 kGy and time of almost 40 minutes (Suppl. Table ST1-Setup 4 and Fig. S3h).

The natural tissue 'texture' created by hypertrophic chondrocytes in calcified cartilage and osteocytic lacunae in subchondral bone is ideal for the reliable measurement of nano-scale load-induced displacements within the intact joint using DVC. For DVC, the 3D texture is correlated between a sequence of snapshots capturing the local movement/distortion of the tissue texture as global load displacements are applied. Therefore, three more advances were made: firstly, synchronising our unique nano-precision joint motion replicator with meticulous built-in rotation into the imaging chain (see Methods); secondly, further reducing the dose (to <25 kGy) and scan time (1.1 min, Suppl. Table ST1- Setup 2, and Fig. S3F), and thirdly,

application of an in-house high accuracy DVC code (Diamond-DVC, see Code Availability below).

The nano-precision joint motion replicator design: was developed by adapting a bespoke nano-precision tension-compression-torsion rig[31,32] (Fig. 1A) that has air-bearing rotation within the load train, enabling continuous sample rotation at high speed (>10 rpm), synchronously with better than 0.001° differential error [see Methods]. Key to avoiding unwanted off-axis forces and misalignment artefacts during sCT was laser alignment of the rams rotating on air-bearings to ensure concentricity to better than 50 nm, or <10% of voxel size. Load measurement accuracy of greater than 0.1 N with 50 nm displacement control was enabled by pre-scanning of joints and 3D printing the grips/cups to ensure alignment was conserved during rotation.

The unique digital volume correlation code: allows flexible point cloud specification of sub-volume locations, concentrating correlation into the regions where displacement values are sought, preventing subvolumes from locating within voids and overlapping surfaces (Fig. 1)[33]. Discrete DVC sub-volume centres were obtained by extracting nodes using unstructured 3D meshing of the joint generated from tomographic data (Figs. 1F, G). Combined with customized image processing, DVC point density was readily modifiable in distinct anatomical joint compartments to allow variable measurement accuracy levels of load-induced strain to be attained (Fig. 1H).

This combination of advances (Fig. 1A,H,K and Fig. 2) allows the generation of 3D full-field displacements in the subchondral bone and calcified cartilage of a whole joint with 240-480 nm precision (0.3 voxel, Fig. 1H). Accuracy was increased further to yield 80-160 nm precision (0.08 voxel) when only the calcified cartilage compartment (which has strong image texture at the micron scale) of the joint was considered (Fig. 1H). This non-invasive measurement of displacement/strain within whole joints under load demonstrates a facility for direct measurement of tissue mechanical response across the articular calcified cartilage/subchondral bone interface (Fig. 1K), enabling integration with existing anatomical and organ scale data as well as validation of multiscale finite element models. When applying loads to whole joints, the deconvolution of the complex 3D interactions between tissue material properties and structure is, however, difficult. They nonetheless demonstrate that the distribution and concentration of displacements (and hence strain) can now be measured across the tibial plateau, even within relatively small areas (<500 μm or <1/8 of the area), as the femur transfers the applied load. Strain can also be further localised in the subchondral trabecular struts of the tibia.

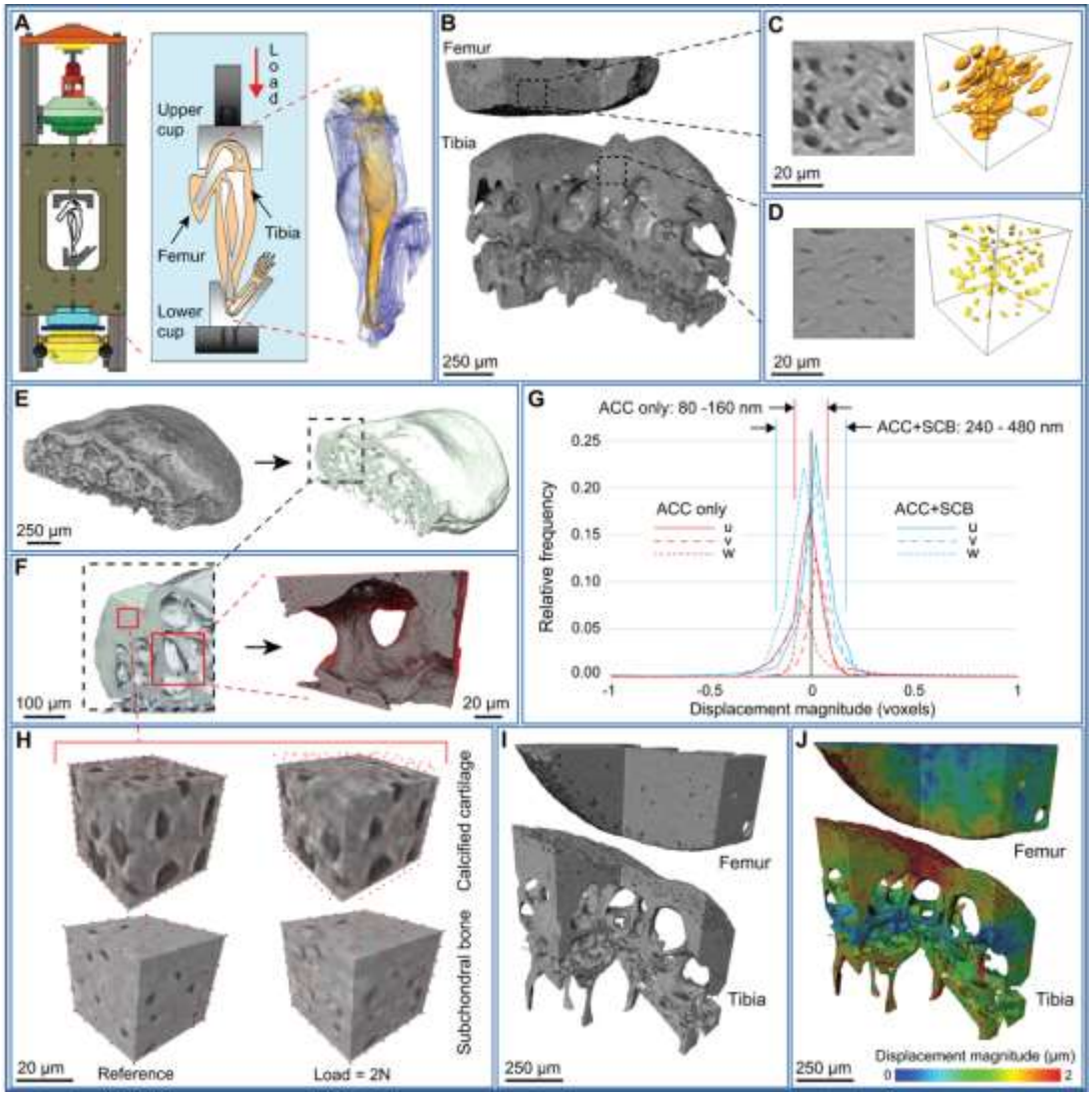

Fig. 1 Ultra-high resolution synchrotron computed tomography (sCT) and digital volume correlation (DVC) of intact joints: (A) Schematic of *in situ* sCT imaging setup (see Suppl. Fig. S1). **(B)** 3D cut-away rendering of sCT data from the medial side of a murine knee joint (STR/Ort 20 week), with **(C)** expanded view from articular calcified cartilage (ACC) region of the femur showing hypertrophic chondrocyte lacunae as dark regions within the sCT data (left) and as rendered voids (right) and **(D)** likewise for osteocyte lacunae from subchondral bone (SCB) region of the tibia. Development of DVC point clouds: **(E)** rendering of the proximal tibia segmented through a region-growing algorithm (left) followed by morphological closure of hypertrophic chondrocyte and osteocyte lacunae (right), and **(F)** expanded views showing subsequent tetrahedral finite element mesh (left) and nodes used as the DVC point cloud (right). **(G)** DVC displacement precision determined from correlation of repeat reference images as +/-1 standard deviation (indicated by vertical lines) of displacement components (u,v,w) in the coordinate (x,y,z) directions: between 80-160 nm for the ACC and 240-480 nm for the entire joint including SCB. Results are representative of n=2 joints. **(H)** Two subvolumes of size 48 voxels (39 µm) in reference (left) and deformed (right) states with red points representing the point cloud for ACC (top) and SCB (bottom) regions (higher density in ACC where strains are higher). **(I)** 3D cut-away rendering of the medial aspect of a STR/Ort 40 week joint illustrating femur (top) and tibia (bottom) morphologies, and **(J)** superimposed displacement magnitude obtained by DVC.

To demonstrate use of the technique to probe how the tibia accommodates loading with even greater precision, an alternative methodology for applying a highly controlled load via a spherical tipped indenter onto the tibial plateau (where osteoarthritic lesions appear most prominently in this strain) was developed (Fig. 2). The indenter allows application of identical, controlled loads to the tibial plateau in both mouse strains at a highly reproducible location, without anatomical or morphological differences that would otherwise complicate interpretation. This enables localised mechanical behaviour, particularly material fracture characteristics, to be probed using region of interest scanning, enabling even higher spatial strain resolution. The joint was disarticulated, and the tibia and its articular cartilage and medial meniscus preserved. This was then mounted and a 200 μm radius tip diamond indenter located directly over the medial plateau. Fig. 2A shows the measured displacements/strains for relevant non-invasive whole joint loading. Fig. 2B demonstrates that indentation introduces no imaging artefacts and the tibia sample is stable, allowing volumetric imaging with resolution suitable for morphological and mechanical response measurements analogous to those for whole joint loading. This technique was then used to apply highly controlled loads in 1 N increments (Suppl. Methods) up to failure. These methods provide data critical to unravelling the relationships between morphological changes and localised mechanical properties across the calcified cartilage and subchondral bone interface in both joints of mice that exhibit healthy ageing and those prone to osteoarthritis (Fig. 2C, discussed below).

Hypertrophic chondrocyte lacunar size in the osteoarthritis-prone joint: Image processing and surface rendering techniques can be applied to 3D images attained using our methodology (Fig. 1 & 2) to effectively measure changes, as well as differences, in articular morphology. For example, we can measure larger hypertrophic chondrocyte lacunar volumes in the calcified cartilage of a 20-week old STR/Ort (osteoarthritic) murine joint (Fig. 3B & F) than in an age-matched control CBA (healthy) joint (Fig. 3A & E). The scope to measure these larger hypertrophic chondrocyte lacunae was also apparent in an ageing 40 week-old osteoarthritic STR/Ort mouse joint (Fig. 3C, D, G, H, I, $P<0.001$) which, at this age, was coupled to a significantly greater thickness in the joint's calcified cartilage tissue layer (Fig. 3J). Direct imaging of intact joints is also useful for revealing greater elongation of these expanded calcified cartilage hypertrophic chondrocyte lacunae in the STR/Ort than in the healthy CBA joints (Fig. 3K – Q, $P<0.01$).

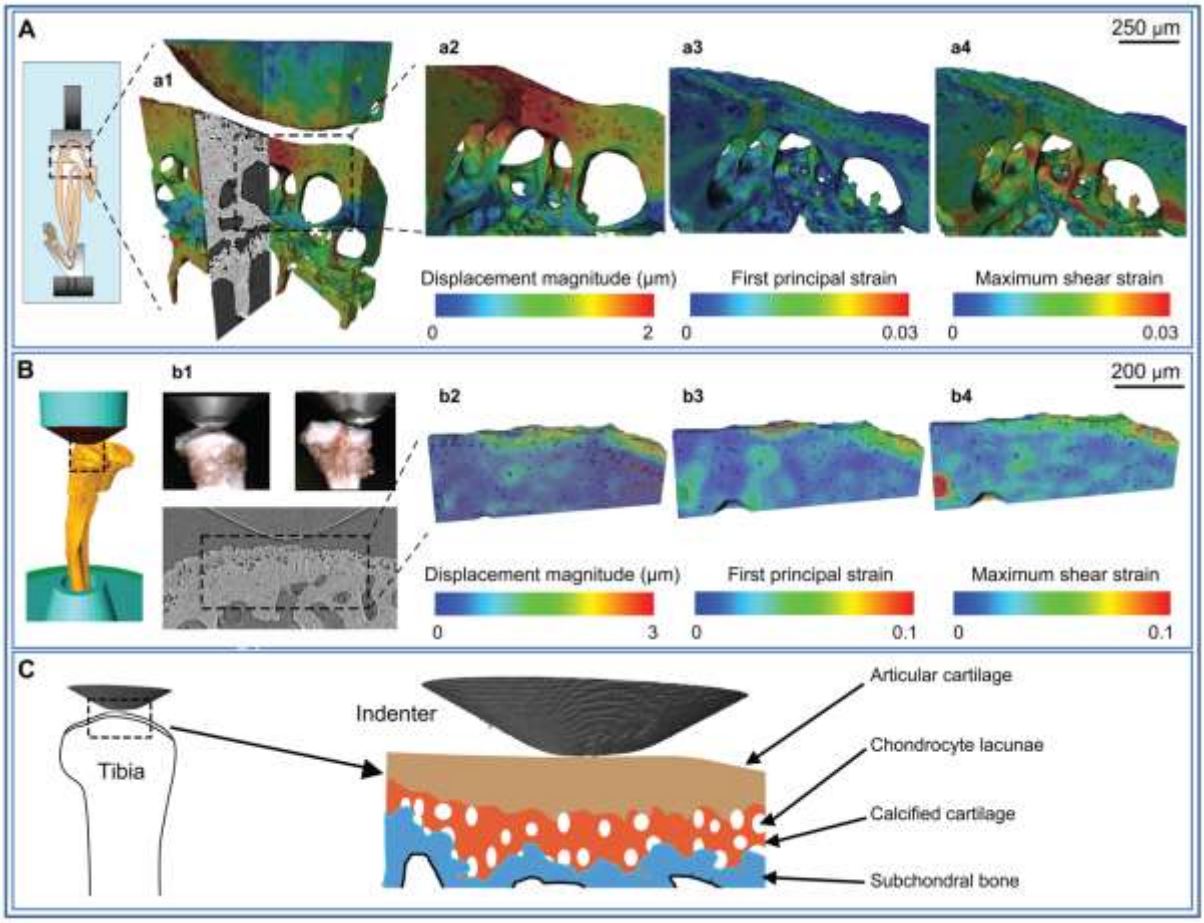

Fig. 2. 3D strain mapping of intact tibia: (A) Schematic of the full mouse joint loading model (left), **(a1)** expanded view showing ultra-high resolution imaging (0.8 µm pixel size) of the medial plateau of a 40 week-old STR/Ort mouse (*n*=1) with superimposed displacement field. Further expanded views of **(a2)** displacement magnitude, **(a3)** first principal strain and **(a4)** shear strain fields. The full joint loading configuration is representative of physiologic loading, and closely recapitulates a common *in vivo* experimental protocol. **(B)** Schematic of indentation loading applied to the disarticulated tibia (left), **(b1)** lateral (left) and posterior (right) views of the 200 µm tip radius diamond indenter in contact with the medial plateau, and (bottom) representative tomography slice under the indenter showing highly-resolved hypertrophic chondrocyte and osteocyte lacunae of a 40 week-old CBA mouse (n=1). Further expanded views of **(b2)** displacement magnitude, **(b3)** first principal strain and **(b4)** shear strain fields within the articular calcified cartilage and subchondral bone regions. Indentation allows highly controlled loading whilst local imaging allows excellent resolution. **(C)** Schematic highlighting the capability of this method to enable ultra-high resolution imaging during highly controlled indentation, with loading transmitted through the articular cartilage and mineralized subchondral layers.

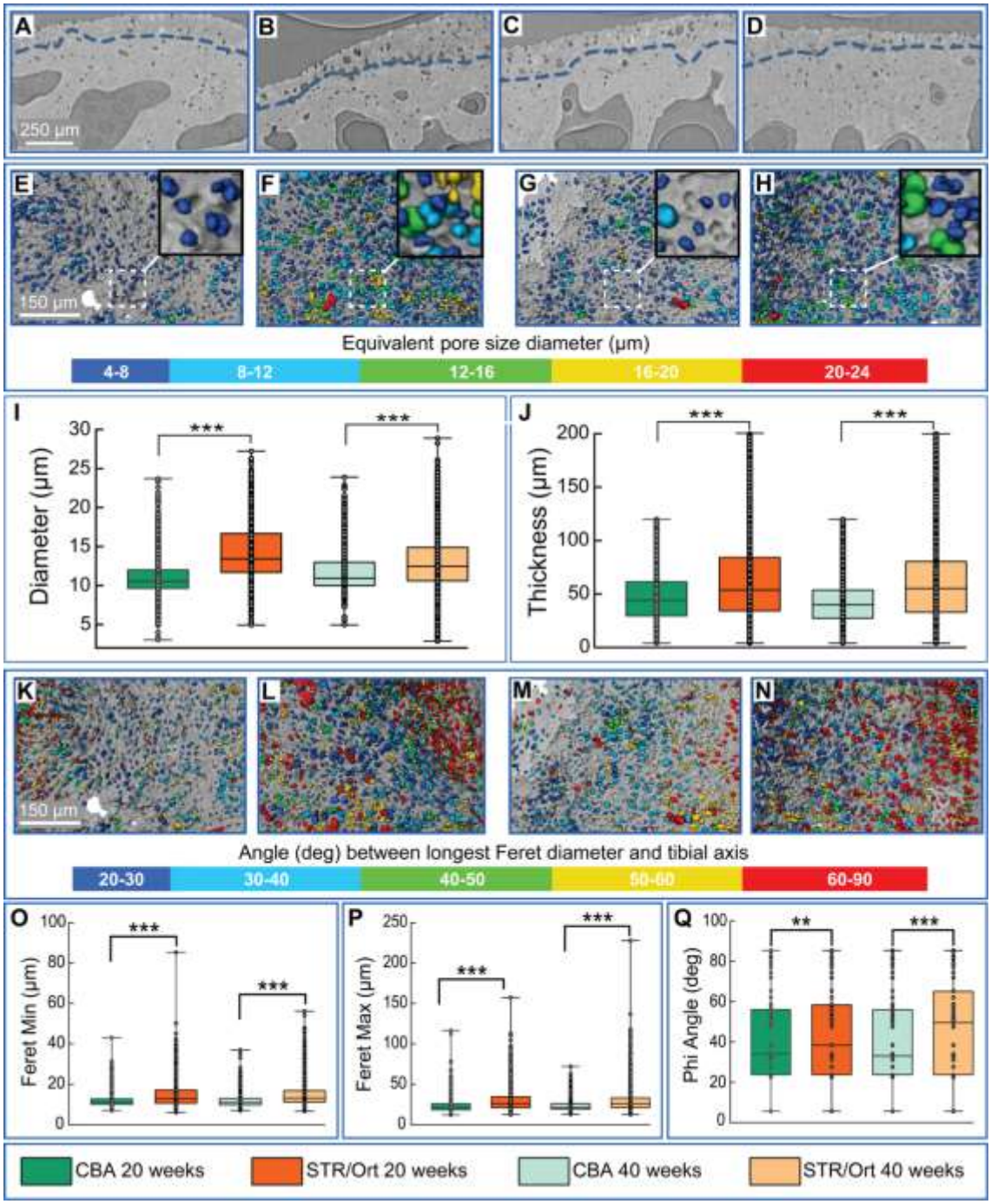

Fig. 3. Ultra-high resolution synchrotron CT imaging of calcified cartilage: Example tomography sections from: **(A)** CBA 20+ week old, **(B)** STR/Ort 20+ week old, **(C)** CBA 40+ week old, and **(D)** STR/Ort 40+ week old. Calcified cartilage chondrocyte lacunae morphology and distribution illustrated for CBA (**E**-20 wk, **G**-40 wk) and STR/Ort (**F**-20 wk, **H**-40 wk), with **(I)** equivalent volume spherical pore diameter and **(J)** calcified cartilage layer thickness quantified. Depiction of angle between longest lacunae dimension (maximum Feret diameter) and tibial axis for CBA (**K**-20 wk, **M**-40 wk) and STR/Ort (**L**-20 wk, **N**-40 wk), with **(O)** smallest dimension, **(P)** largest dimension, and **(Q)** orientation quantified. Box-whisker plots: n=1 joint in each age/strain with n>1000 individual chondrocytes measured in each joint; boxes of 25^{th}/75^{th} percentiles with median bar and whiskers encompass 99% of data points; different from adjacent population with (***) $p<0.001$ and (**) $p<0.01$.

Tissue-specific correlation of microfracture surfaces with strain patterns and morphological features at high spatial resolution: With a view to documenting fracture surfaces, strain patterns and morphological features, we utilized indentation loading to create localized tissue deformation under the medial condyle of tibiae isolated from a healthy, ageing control (40 week-old CBA) and from early and late-stage osteoarthritic joints (20 and 40 week-old STR/Ort; Figure 4). Results show an unprecedented level of detail for localization of deformation and damage in specific subchondral tissues of intact bones. We observed load-induced fracture only within the deep subchondral bone regions of a healthy control tibial condyle, with the calcified cartilage layer remaining structurally intact. DVC strain patterns exhibit high apparent tensile strains associated with the tissue fractures, which can be difficult to otherwise observe. The relationship between fracture surface and nearby osteocyte lacunae is also demonstrated through morphological analysis of the imaging data. In marked contrast, load application in an osteoarthritic 40-week old STR/Ort mouse tibial condyle instead produced fracture surfaces restricted to the calcified cartilage layer, with an orientation parallel to and near the overlying condylar layer. A sample of intermediate age from the osteoarthritic mouse line (20-week old STR/Ort) exhibited intermediate behaviour, with a complex fracture surface spanning the depth of the calcified cartilage, passing through a region of clustered large pores and with high apparent compressive strains. These data, albeit from single representative tibial samples, show that this technique can be used to explore the evolution of damage within sub-articular tissues and whether osteoarthritis susceptibility is linked to greater vulnerability to calcified cartilage cracking. Specific hypotheses concerning load-induced strain can be explored (Figure 4d), with response mapped directly to observable microstructural features. DVC strain measurement will define fracture location, orientation and susceptibility and create a basis for evaluation of microstructural tissue models.

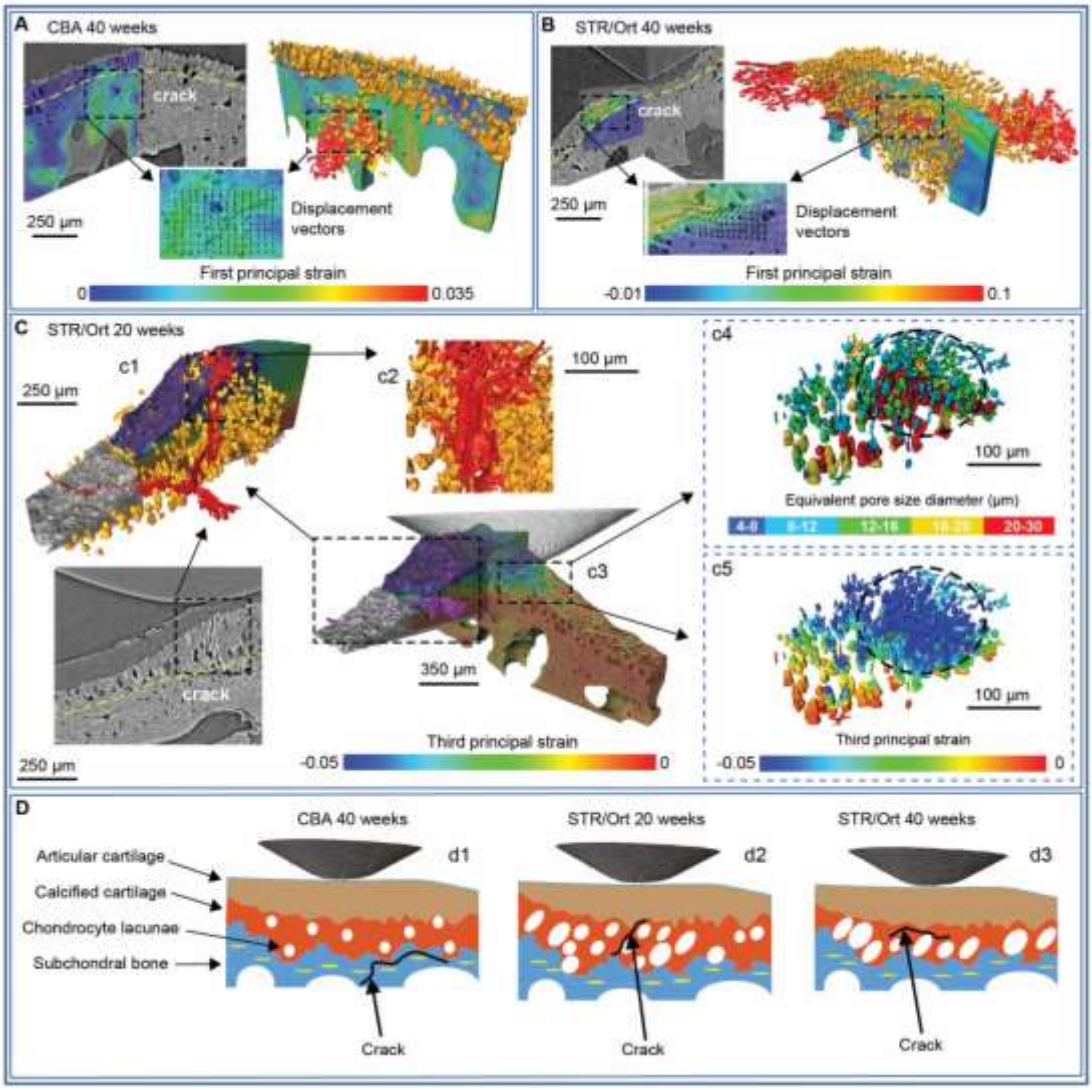

Fig. 4. Correlative visualisation of microstructure, strain patterns, and fracture surfaces: (A) Fracture surfaces (red) appear deep to the articular surface within subchondral bone (below dashed yellow line) in an aged CBA control sample, but **(B)** shallower, within calcified cartilage (above dashed yellow line) in an aged STR/Ort arthritic sample. DVC analysis aids fracture identification (red) with localized patterns of high apparent tensile strain, and highly resolved spatial association with osteocyte (yellow) and chondrocyte lacunae (orange) is demonstrable through morphological analysis. **(C)** A younger 20 week STR/Ort sample exhibits clear fractures through the articular calcified cartilage in tomography sections **(c1, bottom panel)**, as part of a complex fracture surface spanning between subchondral bone and articular cartilage **(c1, c2)**. Portions of the fracture surface **(c3)** pass through clusters of hypertrophic chondrocyte lacunae in calcified cartilage **(c4)** and exhibit high apparent compressive strains **(c5)**. Results represent analysis of n=1/strain/age. **(D)** These multi-faceted measurements support development of detailed tissue function hypotheses: **(d1)** healthy joint: loads transferred through a stable layer of calcified cartilage with small homogenously distributed chondrocyte lacunae, overload fractures within repairable subchondral bone (CBA 40 weeks); **(d2)** early-stage OA: defective transfer of joint loads through larger clustered hypertrophic chondrocyte lacunae, complex trans-calcified cartilage fractures (STR/Ort 20 weeks); and **(d3)** late-stage OA: calcified cartilage thinning and stiffening, with fractures localized to the calcified cartilage/subchondral bone interface (STR/Ort 40 weeks).

Quantification of tissue-level strains during physiologically representative whole joint loading in the STR/Ort mouse model of osteoarthritis progression:

A loading regime was developed to recapitulate steady-state levels achieved during typical use of the flexed-knee model whilst supporting digital volume correlation. Reference images were collected by compressing samples at 5 microns/s to a preload of 1.0±0.1N, waiting 10 minutes for load relaxation, then sCT scanning with sample motion stabilized. Two load steps increasing peak load by 0.2N each were then added, with subsequent relaxation and scanning. Peak loads were then increased into the 2.0 to 2.5 N range for final relaxation and scanning sequences. Relaxed load levels were approximately half of the peak load levels in all cases and were stable within the ±0.1N measurement precision of the loading system. Strain maps (Fig. 5) reflect correlation between the preload and highest applied load scan volumes.

The whole-joint methodology was used in a longitudinal sequence within the STR/Ort line (8, 36 and 60 weeks of age), with a single joint from a mouse at each age/strain evaluated. Tissue compression in the medial tibial plateau (the osteoarthritis-prone condyle in the STR/Ort mouse), as documented through minimum (third) principal strain in Fig. 5A, is high in magnitude prior to osteoarthritis onset (8 weeks) throughout the contact region directly adjacent to the femoral condyle, mostly through the region of articular calcified cartilage with some extension into the subchondral bone. At this age, direct femoral contact dominates the joint compressive loading. By 36 weeks (osteoarthritis) higher magnitude compressive strains are seen predominantly in the articular calcified cartilage and there is also evidence of compliance within the deeper bone trabeculae supporting the tibial subchondral mineralized plate (Fig. 5B). By 60 weeks (advanced osteoarthritis) a very different pattern is observed, with relatively low levels of tissue compression throughout the direct tibial contact region and deeper supporting tissues (Fig. 5C). These data indicate a utility for this technology in revealing general trends in joint tissue mechanics. They pinpoint a need to further study whether the articular construct shifts from a broadly compliant toward a stiffer structure before, during or after onset of osteoarthritis and whether this is also partly recapitulated in healthy, ageing joints.

Our methodology also quantifies tissue tension as evidenced by maximum (first) principal strain. Prior to osteoarthritis onset (8 weeks), highly heterogeneous tissue tension is observed throughout the medial tibial plateau (Fig. 5D) and these tissue tensions become more uniform and decrease in magnitude with osteoarthritis development at 36 weeks (Fig. 5E), and more so at 60 weeks of age (Fig. 5F). The fact that these changes can be measured indicates that the methods allow an examination of the role of microstructure in strain development. Our data also evidence the scope to map these load-induced tissue strains directly to changes in tissue structure. In the samples studied here tissue strain changes are measured in parallel with articular calcified cartilage morphological characteristics measured at high spatial resolution (Fig. 5G). Our observations of nano-scale resolved strains in intact loaded joints also allow emerging high tensions at the tibial insertion of the anterior cruciate ligament prior to osteoarthritis onset to be examined (8 weeks; Fig. 1D) (arrow). With osteoarthritis development at 36 and 60 weeks, this region of tensile strain has expanded (Fig. 5E & F) and dominates the strain pattern.

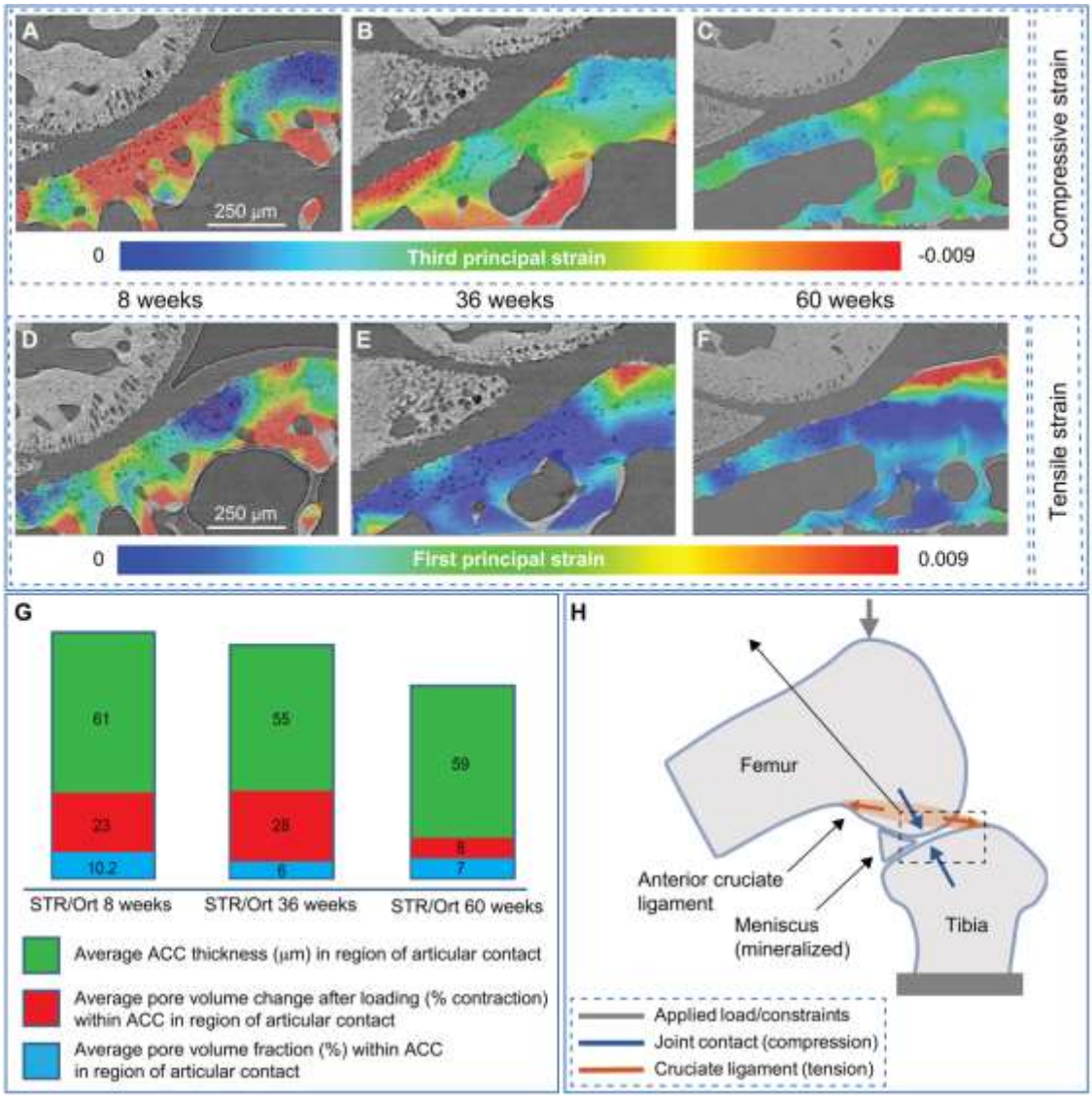

Fig. 5. Nano-resolved strain under physiologically representative loading prior to and after the onset of osteoarthritis: (A,D) STR/Ort 8+ week, (2.4/1.2±0.1N), prior to onset of osteoarthritis (B,E) STR/Ort 36+ week, (2.4/1.4±0.1N), post osteoarthritis onset, and (C,F) STR/Ort 60+ week, (2.2/1.2±0.1N), advanced osteoarthritis. Applied loads are shown as (peak/relaxed ±1 standard deviation), with preloads for strain measurement of 1.0/0.5±0.1N. A single joint from a mouse at each age/strain was evaluated. (A-C) Tissue compression (third principal strain) evolves during different stages of osteoarthritis progression. (A) Distributed strain under the femoral condyle that permeates throughout the articular calcified cartilage and into the subchondral bone in the knee joint of an 8 week-old mouse. (B) At 36 weeks, compression localizes more, shifting to a location adjacent to the now hypertrophied mineralized meniscus. (C) By 60 weeks the pattern is very different, with relatively low levels of tissue compression throughout the direct tibial contact region and deeper supporting tissues. (D-F) Tissue tension (first principal strain) also evolves with age. Magnitudes are initially high in the articular contact regions, but low at 36 weeks and beyond. In contrast the anterior cruciate ligament location on the tibial plateau exhibits low magnitude tensile strain initially followed by a higher magnitude and more expansive region as age increases. (G) Articular calcified cartilage (ACC) thickness, the average chondrocyte lacunae pore volume, and the change in chondrocyte lacunae pore volume under load. (H) Schematic of the standard loading model used.[34]

Discussion

Our methodology bridges the gap between whole joint mechanics and nanoscale strain measurement in sub-articular tissues, which will allow the elusive structural cartilage-bone features underpinning joint health to be defined. These techniques can clearly be used to reveal hierarchical changes in tissue structure and mechanical behaviour. They show that it is possible to examine whether strategies for adapting to physiologically representative mechanical joint loading diverge in diseased joints and that early changes in calcified cartilage structure are worthy of study, as they may prefigure disease onset. These data provide the enabling technology for the role of sub-hyaline mineralized tissue microstructure in strain development to be explored. They also signpost a specific and vital mechanical role for stiffening in this calcified cartilage layer in disease progression (Fig. 5).

A major challenge in osteoarthritis research is understanding the intimate interactions between the adjoining joint tissues. This challenge is perhaps most obvious, specifically in the biological and physical crosstalk between the articular cartilage and subchondral bone, where the calcified cartilage layer is found sandwiched[35]. Indeed studies have shown that this crosstalk can be facilitated by vessels reaching from the subchondral bone into the calcified cartilage; patches of uncalcified hyaline cartilage being in contact with the subchondral bone, and microcracks and fissures extending through the osteochondral unit[36]. Previous studies have either scanned and examined deformation and ensuing crack formation in a single bone at the micron scale[37] or have probed surface and near-surface mechanical properties at the nano-scale in isolated tissue segments[20]; our technique allows the direct measurement of mechanical strains in intact joints under controlled and physiologically realistic loading conditions. Several studies have used diffraction or small-angle X-ray scattering to measure strain, but again this was only achievable in extracted bone fragment samples[38,39] .

Our studies have gleaned information across the entire osteochondral unit by combining the use of two joint loading protocols - an indenter and a non-surgical knee joint loading model – together with ultra-high resolution imaging of intact mouse knee joints from control and osteoarthritis-prone strains. The indenter protocol allows application of identical, controlled loads to the murine tibial plateau at a highly reproducible location, without anatomical or morphological differences that would otherwise complicate interpretation. The large radius indenter (with respect to tibial plateau curvature) therefore allows more controlled and consistent probing of localized mechanical response. It is recognised that the precise tilt (angle or articulation) of the tibial plateau does show some variation between samples, and that this may be a factor contributing to tissue strain development. We used a vertical orientation of the indenter and contact with the middle of the tibial plateau as a means of creating consistent force input into the samples and to allow the effects of multiple geometric and material influences to manifest without attempts to adjust for any particular factor. Future studies using our method described herein will enable the material property and geometry influences on tissue strain to be examined.

Whilst the hierarchical structural and mechanical properties of the adjoining joint tissues are known to be dissimilar[40], there is currently little awareness of how tissue strains manifest or whether mechanical properties across the osteochondral unit vary during healthy and pathological ageing of the joint. The calcified cartilage is clearly crucially located, linking the underlying, extensively vascularised subchondral bone through a mineralised interface with discontinuous, unmatched, collagen type I and II fibres, to the hyaline cartilage where a continuous traverse of collagen type II fibres abruptly transition from calcified into overlying non-mineralised cartilaginous tissue. The calcified cartilage is approximately 100 times stiffer than the overlying hyaline cartilage and 10 times less stiff than the underlying subchondral bone[41,42]. It is therefore unsurprising that the calcified cartilage layer is thought to be integral

to load transmission from the compliant hyaline cartilage, to the underlying stiff subchondral bone[42]. Indeed alterations in the calcified cartilage thickness, represented by the balance between the rate of tidemark advancement into the hyaline cartilage and the rate of calcified cartilage resorption at the osteochondral interface, are associated with increased risk of joint injury[43]. Our technique was also applied to healthy murine joints, allowing load-induced strain localisation to be measured in the joint calcified cartilage and underlying subchondral bone (Fig. 5). Our technology permits examination of key questions: is joint function safe-guarded by the calcified cartilage? Does joint health rely on structural robustness at its two interfaces? Whilst these principles would be innovative, they are nonetheless consistent with previous data showing the role of the calcified cartilage in preserving the structural integrity of the articular cartilage and in regulating subchondral bone mass and architecture.

The stiffness gradient from the subchondral bone to the calcified cartilage may be attributed to mineralisation status. Reports of lower subchondral bone mineralisation and stiffness have indeed been reported in osteoarthritis[44-48] and, similarly, alterations in the stiffness gradient from the calcified cartilage to the subchondral bone are observed at the macro-level in association with early degenerative changes[42]. Our data suggest that the transfer of high joint loads to the underlying subchondral bone should be examined further as a potential means by which healthy joint architecture is preserved; this is consistent with high vascularisation and scope for rapid and ordered remodelling of subchondral bone. The effectiveness of this transfer of high joint loads to the subchondral bone is also consistent with our findings indicating selective, longer term increases in subchondral plate thickness at these loaded joint locations *in vivo*[49]. Our methods also allow localised inhomogeneity in the strains to be observed, with some regions exhibiting strains much higher than the nominal, homogenized values that traditional testing reveals. This is consistent with both measurement and modelling of mechanical response to load across a broad range of hierarchical scales within bone and other biological tissues[20,50]. As our measurements are more spatially resolved than prior work, this broad distribution of strain magnitudes is not unexpected.

The presence of cracks in the joint calcified cartilage has been recognised for some time, however their significance had remained undetermined[51]. It has been postulated that microcracks in the osteochondral interface may enable the transfer of molecules and substances to the hyaline cartilage, from which it is normally protected[52,53]. For example, subchondral-derived inflammatory cytokines and growth factors that have been shown to be detrimental to chondrocyte health[35]. The thickness and porosity of the cartilage and bone in both human and equine samples also influences bone-cartilage interface transfer[54]. Furthermore, microcrack propagation may also contribute to the mechanical failure of the joint when placed under high loads, as has been shown in Thoroughbred horse joints[55]. The hypothesis that greater levels of calcified cartilage chondrocyte hypertrophy predispose greater strain concentration, load-induced microcracking and osteoarthritis, is underpinned by our studies.

The idea that mechanical failure may indeed occur in close proximity to the calcified cartilage has recently been supported by the seminal description of hyperdense mineralised protrusions (HDMP) from the subchondral plate in joints from Thoroughbred racehorse and more recently in human osteoarthritic hips[56-59]. These HDMPs comprise a hypermineralised infill material which may be an extension of a crack self-healing mechanism observed in bone[60]. Our technique described herein will enable the tracking of strain fields during HDMP development to potentially validate their proposed method of formation.

Mechanics and genetics are prime determinants of healthy joint ageing. Links to genetic selection for rapid growth also exist[61] and recent research has prompted speculation that hyaline cartilage chondrocytes ‘switch’ from an inherently stable to a transient phenotype,

similar to that observed in the growth cartilage[62-64]. This transience, vital for longitudinal bone growth, contrasts however with the stable hyaline chondrocyte phenotype required to assure life-long joint integrity. The data we have presented herein examining hypertrophic chondrocyte lacunae size conform with other studies highlighting a contribution of phenotype switching to the demise of the joint and is consistent with our previous work which investigated the expression of molecular markers of chondrocyte hypertrophy in these STR/Ort mice[63]. This revealed an expected pattern of type X collagen expression in the unaffected (lateral) condyles of STR/Ort mouse joints, with immunolabeling restricted to hypertrophic chondrocytes. Consistent with our data here, an increased type X collagen immunolabeling was observed throughout the medial (affected) condylar articular cartilage matrix in 8–10-week-old STR/Ort mice, before histologically detectable osteoarthritis. Also, consistent with our findings here, an additional marker of chondrocyte hypertrophy, MMP-13, was detected to be increased in the calcified cartilage chondrocytes of STR/Ort mice[63]. Together these data warrant further investigation into the role of chondrocyte hypertrophy in the calcified cartilage in generating the abnormal strain localisation observed in osteoarthritic joints. Interlinks between these discordant phenotypes are however not fully deciphered and whilst the hypothesis that limited 'switching' contributes to preserving joint health is controversial, our methodology will undoubtedly provide clear insights into the mechanical role of chondrocyte hypertrophy in osteoarthritis.

The utility of our whole loaded joint imaging and DVC approach is perhaps best exemplified by the generation of unique, 3D full-field displacements and strains in the intact mineralised joint tissues (Fig. 5), indicating potential for future studies examining the interplay between genetics and mechanics in joint health and osteoarthritis. Our findings provide a means for generating hypotheses in significant orthopaedic healthcare challenges such as osteoarthritis, as we have done here. However, one limitation of our study is the difficulty in obtaining data from a large number of replicate animal joints for statistical validation of these hypotheses, as synchrotron access for performing ultra-high resolution *in situ* imaging is limited. The technique we have developed will nonetheless have a wide range of applications, for example, in orthopaedics measuring strain in both healthy joints and the impact of joint replacements on strain distributions. For osteoarthritis, these insights provide a viable model system for the efficacy of treatments to be explored in longitudinal studies, potentially shortening the drug development pipeline. They also expand studies across the length scales, from nanoscale resolution of the osteochondral unit to the whole joint. Further, the technique is applicable to many non-biological systems where strain measurements are required at the nano-scale with minimal radiation damage *in situ* or operando.

Methods

Animals

Male STR/Ort (bred in-house at the Royal Veterinary College) were examined before osteoarthritis onset (8 weeks), at early osteoarthritis onset (20 weeks) and late osteoarthritis (40 weeks) in comparison to male age-matched CBA mice (Harlan UK Ltd. UK). CBA mice are the most appropriate control for the STR/Ort mouse as they are the nearest available parental strain, and extensive analysis reveals they show no overt signs of osteoarthritis with ageing[29]. Mice were kept in polypropylene cages, with light/dark 12-h cycles, at 21 ± 2°C, and fed ad libitum with maintenance diet (Special Diet Services, Witham, UK). All procedures complied with Animals (Scientific Procedures) Act 1986, were approved by the local ethics committee of the Royal Veterinary College, and comply with the ARRIVE guidelines. STR/Ort mice were maintained by brother/sister pairing[29]. Whole hind limbs were dissected and stored frozen at -20°C. Knee joints were either scanned as intact limbs, or were dislocated on the day

of scanning, all soft tissues removed from the distal tibial element before it was severed close to the midshaft with a bone saw. All samples, both intact joints and disarticulated indentation samples, were maintained hydrated in phosphate buffered saline during all scanning[29].

In situ testing using bespoke nano-precision rig

Our bespoke in situ mechanical rig[65] (P2R; Fig.1 and Suppl. Fig. S1) was designed with a granite base frame, two rotation shafts coupled with air bearings and servomotor assemblies, a load measurement system and its associated drive specifically for in situ X-ray tomography studies[31,32,66]. Full details are in Supplementary Methods, with only key attributes detailed here. The air bearings ensure frictionless axial movement of shafts engineered for permanent alignment accuracy of better than 50 nm, which is required during scanning to avoid misalignment artefacts and unwanted off-axis forces. Rotation shaft ends are fixed to pre-aligned micrometre-resolution X-Y translation stages (T12XY, Thorlabs) and aligned specimen (intact knee joint) are biofilm-sealed to limit dehydration and loaded using custom-built, 3D printed plastic cups designed to allow axial compression with sub-micron precision displacement steps to be applied across a flexed knee joint[67].

For dislocated tibias, the mid-shaft was embedded in 1.5 mm of acrylic resin in the pre-aligned lower cup[68] and specimens indented from above on the centre of the tibial medial plateau using a 120^{o} diamond Vickers indenter with a 200 μm radius tip (Gilmore Diamond Tools, Inc.) with 10 micron displacement steps applied and measured loads reaching a maximum of 4N (note in the whole joint experiments 20 micron displacements were used). A fifteen minute-window was allowed after loading to avoid motion artefacts during scanning caused by stress relaxation. All the tests were carried out in wet conditions using a phosphate buffered solution (PBS)-filled environmental chamber placed in the P2R rig.

Ultra-high resolution, fast pink beam imaging

Ultra-high resolution imaging during indentation of the tibia and compression of intact joints under realistic loading conditions was performed using the Diamond-Manchester Imaging Branchline I13-2[69,70] of the third-generation synchrotron Diamond Light Source. Traditionally, monochromatic X-rays have been used for phase contrast enhanced images of bone[27,71,72]; instead we used a 'pink beam' to enable similar data quality with shorter acquisition times. Sample deformation represents a major obstacle to high-resolution tomography for joints under compression, and rapid imaging with a pink beam was essential to enabling this. Here the spectral distribution is determined by the design of the synchrotron, the insertion device (ID) settings and the choice of filters and mirrors. The resulting beam (once filtered as below) at I13-2 is ~100 times more intense than a monochromatic beam generated by a monolayer monochromator[30]. We used the Diamond mini-beta undulator (2 m long U22 undulator, 2.2cm period length) from which radiation from 90 periods interferes coherently to produce sharp peaks at harmonics of the fundamental frequency (Suppl. Fig. S3a). Using a 5 mm ID gap (deflection K~1.743), X-rays of 5-30 keV and flux density of about 〖6x10〗 ^13 ph/s/ 〖mm〗 ^2 (flux simulations are detailed in Supplementary Methods) were generated. Radiation was then selectively filtered to attenuate low energy X-rays, protecting instrumentation and reducing tissue radiation dose. Filters were used (C-1.3 mm, Al-3.2 mm, and Ag-75 μm) to tune the flux to about 〖4x10〗 ^11 ph/s/ 〖mm〗 ^2, using 6 harmonics between 16 and 25 keV (Suppl. Fig. S3a), approximately 10 times more than the monochromatic flux (setup 4, E=19 keV, see Suppl. Table ST1). Here, our strategy is to use less photons at lower energies to reduce the mean energy imparted to the tissue by ionizing radiation. We satisfied these requirements by suppressing most of the harmonics below 19 keV (Suppl. Fig. S3b). Slits were

used to truncate the beam just outside the field of view; this reduces both sample exposure and the intensity of noise arising from scintillator defects. We collected in fly-scan mode up to 4001 high-count projections with a transmission between 20-40% (effective pixel size of 1.6 µm using setup 1 and 0.8 µm using setup 3, see Suppl. Table ST1) in less than 7.3 minutes, by means of our precise mechanical rig with built-in rotation coupled to a fast, high dynamic range pco.edge 5.5 camera (16 bit, 100 fps) mounted on a scintillator-coupled microscope of variable magnification.

Radiation dose

A method was developed to measure the signal-to-noise ratio (SNR) from the images and evaluate the radiation dose from the simulated flux[73] (see Supplementary Methods). Prior to analysis, our simulations were compared with flux experiments obtained on the Diamond-Manchester Imaging Branchline and a good agreement was obtained (Suppl. Fig. S4). The dose rate ranges between 0.4-0.5 kGy/s, which is in the range of dose rates obtained at different synchrotron locations (Suppl. Table ST2). The trade-off between scanning time, SNR, and total dose is depicted in Suppl. Fig. S3c-f. The total dose for each tomogram ranges from 100 kGy (setup 1) to 240 kGy (setup 2) for a 4-7 minute scan time, which is above the acceptable irradiation levels for in situ bone mechanics[27]. For comparison, our equivalent monochromatic beam setup (Suppl. Table ST1, setup 3) had a total dose of about 157 kGy/tomogram but the scanning time is 5 times higher and the SNR 3 times lower (Suppl. Table ST1 and Fig. S3h). Reducing the number of projections to 600 in pink beam (~1.1 minute scan time, Suppl. Table ST1 - Setup 2) reduces total dose to 27 kGy/tomogram (Suppl. Fig. S3e) such that hypertrophic cells are still resolvable but osteocyte lacunae are progressively lost (Suppl. Fig. S3c, d, e).

Data processing prior to Digital Volume Correlation (DVC)

Reconstruction was performed with the tomography reconstruction module of Dawn 1.7[74,75], with normalisation (forty flatfield and darkfield images) and ring artefact suppression prior to filtered back projection. Prior to DVC analysis, the tomograms were cropped, normalised and 3D median filtered (kernel size 2). Input to the 3D texture correlation texture algorithm consists of two 8-bit image volumes (non-deformed/deformed) and a flexible point cloud file that specifies the subvolume locations where displacement values are sought. We developed a method to generate discrete DVC points analogous to the nodes where a displacement-based FEA (finite element analysis) calculates displacement results (Fig. 1). Images were imported into Avizo 9.0 software to create binary region of interest masks (femur/ tibia in intact joints and calcified cartilage/subchondral bone in the indent specimens). Masks were obtained by image processing using a region-growing algorithm and then a morphological closure process to fill porosity from subchondral bone and calcified cartilage (Fig. 1E). Images were then eroded by 8 voxels to avoid surface edge effects during the correlation process and then used to generate unstructured tetrahedral finite element (FE) meshes (Fig. 1F) by the well-defined methodology[76]. Finally, mesh nodes were extracted to define the point cloud (Fig. 1G) and high density points created to capture high strain gradients.

Nanoscale displacements extracted from DVC

3D displacement vector fields were calculated using the diamond.dvc open access code[25,33]. A Gauss–Newton minimization is applied with cubic spline volumetric image interpolation to an objective function, defined as the normalised squared differences between subvolumes in the non-deformed and deformed image data, allowing displacements to be measured with subvoxel accuracy. To assess the *a priori* performance of DVC analysis, correlation of repeat reference images was performed (Fig. 1H) with standard deviation of measured displacement vector components used to quantify precision and allow adjustment for imaging noise and

heterogeneous texture. There is generally trade-off between measurement uncertainty and resolution (Suppl. Fig. S3i) and 40-50 voxels subvolume size (32-40 µm) produced the best compromise with a 0.3 voxel DVC accuracy, if the point cloud is homogenously distributed; 0.8-1.6 µm pixel size allowed displacements in subchondral bone and calcified cartilage to be measured with 240-480nm accuracy. Regardless of dose, accuracy was increased to 0.08 voxel (~80-160 nm precision) if only calcified cartilage was considered (Fig. 1H, Suppl. Table ST1 and Suppl. Figs. S3c-f).

A critical step in all DVC methods is selection of an accurate starting point in the vicinity of a global minimum and avoidance of secondary local minima[33]. To redress this, raw images in non-deformed and deformed states were co-registered using a robust iterative optimization algorithm (Avizo 9.0) to remove the rigid body motion (translation and rotation). Each deformed image was then registered with the reference image using the diamond.dvc code. Correlation quality was assessed by reference to magnitude of the objective function returned by the correlation process. Histograms of normalised correlation revealed very low and tightly grouped residuals, indicative of a good match. Point cloud location displacements were interpolated at a set of grid points using Delaunay triangulation and all Green-Lagrange strain components were computed using a centred finite differences scheme. The code modules for strain calculations were modified (from [77]) to include the scattered point interpolation and all the principal strain components.

Statistical analysis

Normality and homogeneity of variance of all the data were checked, and two-sided one-way ANOVA conducted to compare groups. $p < 0.05$ was considered to be significant and noted as *; p-values of <0.01 and <0.001 were noted as ** and ***, respectively. In situ indentation experiments were performed on two different 20-week STR/Ort mice, at four loading steps. Similar strain patterns in the calcified cartilage are found for the two specimens (see Suppl. Fig. S5a). Higher magnitude compressive strains are seen predominantly in the articular calcified cartilage. The strain histograms of the first and third principal strains are similar and appear as asymmetrical distributions (Suppl. Fig. S5b). Animations showing the progressive compression of the hypertrophic chondrocytes in a transverse section are available for visualisation in Suppl. Video SV2.

Data availability

A representative sample of research data from the experiments along with the plot data for the graphs in this manuscript is provided in supplementary material. The underlying data are not provided online due to their size but are available on reasonable request from the corresponding authors.

Code availability

The custom digital volume correlation code used in this study is available at https://zenodo.org/record/3228175#.XZdBRkZKguE.

Acknowledgements

We are grateful to Professor Roger Mason (Imperial College London, UK) for providing our original STR/Ort mice and for advice on their use. We thank Loic Courtois, Steven Van Boxel, Catherine Disney, Gowsihan Poologasundarampillai, Jin He, David Eastwood, Kazimir Wanelik, Ulrich Wagner and Jon Thompson for their help during the beamtimes. We gratefully acknowledge the Engineering and Physical Sciences Research Council (grants EP/I02249X/1, EP/M009688/1), Arthritis Research UK (grant 18768) and MRC (MR/R025673/1). Facilities and research support were provided by the Diamond-Manchester Branchline (I13-2) at

Diamond Light Source (Beamtimes MT13237-1, MT11076-1, MT5003-1), and the Research Complex at Harwell.

Author contributions

Conception and design of the study: PDL, AAP, KM, KAS and BB. Acquisition of data: KM, BB, HG, BJ, KAS, AJB. Interpretation of data, revising the manuscript and final approval, and agreement to be accountable for all aspects of the work: all authors. Drafting the manuscript: KAS, KM, BB, AAP, PDL.

Competing interests.

All authors declare no competing financial interests.

References

1 Denk, W. & Horstmann, H. Serial block-face scanning electron microscopy to reconstruct three-dimensional tissue nanostructure. *PLoS biology* **2**, e329 (2004).

2 Georgiadis, M., Mueller, R. & Schneider, P. Techniques to assess bone ultrastructure organization: orientation and arrangement of mineralized collagen fibrils. *Journal of the Royal Society Interface* **13**, 20160088 (2016).

3 Pabisch, S., Wagermaier, W., Zander, T., Li, C. & Fratzl, P. in *Imaging the Nanostructure of Bone and Dentin Through Small- and Wide-Angle X-Ray Scattering* Vol. 532 *Methods in enzymology* 391-413 (Elsevier, 2013).

4 Zhu, F.-Y. *et al.* 3D nanostructure reconstruction based on the SEM imaging principle, and applications. *Nanotechnology* **25**, 185705 (2014).

5 Gupta, H. S. *et al.* Cooperative deformation of mineral and collagen in bone at the nanoscale. *Proceedings of the National Academy of Sciences* **103**, 17741-17746 (2006).

6 Tadano, S., Giri, B., Sato, T., Fujisaki, K. & Todoh, M. Estimating nanoscale deformation in bone by X-ray diffraction imaging method. *Journal of biomechanics* **41**, 945-952 (2008).

7 Orgel, J. P., Irving, T. C., Miller, A. & Wess, T. J. Microfibrillar structure of type I collagen in situ. *Proceedings of the National Academy of Sciences* **103**, 9001-9005 (2006).

8 Gautieri, A., Vesentini, S., Redaelli, A. & Buehler, M. J. Hierarchical structure and nanomechanics of collagen microfibrils from the atomistic scale up. *Nano letters* **11**, 757-766 (2011).

9 Dierolf, M. *et al.* Ptychographic X-ray computed tomography at the nanoscale. *Nature* **467**, 436-439 (2010).

10 Giannuzzi, L. A., Phifer, D., Giannuzzi, N. J. & Capuano, M. J. Two-dimensional and 3-dimensional analysis of bone/dental implant interfaces with the use of focused ion beam and electron microscopy. *Journal of Oral and Maxillofacial Surgery* **65**, 737-747 (2007).

11 Schneider, P., Meier, M., Wepf, R. & Müller, R. Serial FIB/SEM imaging for quantitative 3D assessment of the osteocyte lacuno-canalicular network. *Bone* **49**, 304-311 (2011).

12 Boyde, A. & Jones, S. J. Scanning electron microscopy of bone: instrument, specimen, and issues. *Microscopy research and technique* **33**, 92-120 (1996).

13 Song, M. J., Dean, D. & Tate, M. L. K. In situ spatiotemporal mapping of flow fields around seeded stem cells at the subcellular length scale. *PLoS one* **5**, e12796 (2010).

14 Roeder, B. A., Kokini, K., Robinson, J. P. & Voytik-Harbin, S. L. Local, three-dimensional strain measurements within largely deformed extracellular matrix constructs. *Journal of biomechanical engineering* **126**, 699-708 (2004).

15 Sztefek, P. *et al.* Using digital image correlation to determine bone surface strains during loading and after adaptation of the mouse tibia. *Journal of biomechanics* **43**, 599-605 (2010).
16 Hoc, T. *et al.* Effect of microstructure on the mechanical properties of Haversian cortical bone. *Bone* **38**, 466-474 (2006).
17 Bay, B. K. Texture correlation: a method for the measurement of detailed strain distributions within trabecular bone. *Journal of Orthopaedic Research* **13**, 258-267 (1995).
18 Nicolella, D. P., Moravits, D. E., Gale, A. M., Bonewald, L. F. & Lankford, J. Osteocyte lacunae tissue strain in cortical bone. *Journal of biomechanics* **39**, 1735-1743 (2006).
19 Katsamenis, O. L., Chong, H. M., Andriotis, O. G. & Thurner, P. J. Load-bearing in cortical bone microstructure: Selective stiffening and heterogeneous strain distribution at the lamellar level. *Journal of the mechanical behavior of biomedical materials* **17**, 152-165 (2013).
20 Tai, K., Dao, M., Suresh, S., Palazoglu, A. & Ortiz, C. Nanoscale heterogeneity promotes energy dissipation in bone. *Nature materials* **6**, 454-462 (2007).
21 Hassenkam, T. *et al.* High-resolution AFM imaging of intact and fractured trabecular bone. *Bone* **35**, 4-10 (2004).
22 Thurner, P. J. *et al.* Imaging of bone ultrastructure using atomic force microscopy. *Modern research and educational topics in microscopy*, 37-48 (2007).
23 Pan, B. & Wang, B. A flexible and accurate digital volume correlation method applicable to high-resolution volumetric images. *Measurement Science and Technology* **28**, 105007 (2017).
24 Hussein, A. I., Barbone, P. E. & Morgan, E. F. Digital volume correlation for study of the mechanics of whole bones. *Procedia IUTAM* **4**, 116-125 (2012).
25 Bay, B. K., Smith, T. S., Fyhrie, D. P. & Saad, M. Digital volume correlation: three-dimensional strain mapping using X-ray tomography. *Experimental mechanics* **39**, 217-226 (1999).
26 Roberts, B. C., Perilli, E. & Reynolds, K. J. Application of the digital volume correlation technique for the measurement of displacement and strain fields in bone: a literature review. *Journal of biomechanics* **47**, 923-934 (2014).
27 Barth, H. D., Launey, M. E., MacDowell, A. A., Ager III, J. W. & Ritchie, R. O. On the effect of X-ray irradiation on the deformation and fracture behavior of human cortical bone. *Bone* **46**, 1475-1485 (2010).
28 Currey, J. D. *et al.* Effects of ionizing radiation on the mechanical properties of human bone. *Journal of Orthopaedic Research* **15**, 111-117 (1997).
29 Staines, K. A., Poulet, B., Wentworth, D. N. & Pitsillides, A. A. The STR/ort mouse model of spontaneous osteoarthritis–an update. *Osteoarthritis and cartilage* **25**, 802-808 (2017).
30 De Fanis, A., Pešić, Z., Wagner, U. & Rau, C. Fast X-ray imaging at beamline I13L at Diamond Light Source. *Journal of Physics: Conference Series* **425**, 192014 (2013).
31 Karagadde, S. *et al.* Transgranular liquation cracking of grains in the semi-solid state. *Nature communications* **6**, 8300 (2015).
32 Kareh, K., Lee, P., Atwood, R., Connolley, T. & Gourlay, C. Revealing the micromechanisms behind semi-solid metal deformation with time-resolved X-ray tomography. *Nature communications* **5**, 4464 (2014).
33 Bay, B. K. Methods and applications of digital volume correlation. *The Journal of Strain Analysis for Engineering Design* **43**, 745-760 (2008).

34 De Souza, R. L. *et al.* Non-invasive axial loading of mouse tibiae increases cortical bone formation and modifies trabecular organization: a new model to study cortical and cancellous compartments in a single loaded element. *Bone* **37**, 810-818 (2005).

35 Goldring, M. B. & Goldring, S. R. Articular cartilage and subchondral bone in the pathogenesis of osteoarthritis. *Annals of the New York Academy of Sciences* **1192**, 230-237 (2010).

36 Lories, R. J. & Luyten, F. P. The bone–cartilage unit in osteoarthritis. *Nature Reviews Rheumatology* **7**, 43-49 (2011).

37 Müller, R. Hierarchical microimaging of bone structure and function. *Nature Reviews Rheumatology* **5**, 373-381 (2009).

38 Yamada, S., Tadano, S. & Fujisaki, K. Residual stress distribution in rabbit limb bones. *Journal of biomechanics* **44**, 1285-1290 (2011).

39 Gupta, H. S. *et al.* Nanoscale deformation mechanisms in bone. *Nano letters* **5**, 2108-2111 (2005).

40 Campbell, S. E., Ferguson, V. L. & Hurley, D. C. Nanomechanical mapping of the osteochondral interface with contact resonance force microscopy and nanoindentation. *Acta biomaterialia* **8**, 4389-4396 (2012).

41 Mente, P. & Lewis, J. L. Elastic modulus of calcified cartilage is an order of magnitude less than that of subchondral bone. *Journal of Orthopaedic Research* **12**, 637-647 (1994).

42 Hargrave-Thomas, E., van Sloun, F., Dickinson, M., Broom, N. & Thambyah, A. Multi-scalar mechanical testing of the calcified cartilage and subchondral bone comparing healthy vs early degenerative states. *Osteoarthritis and cartilage* **23**, 1755-1762 (2015).

43 Doube, M., Firth, E. & Boyde, A. Variations in articular calcified cartilage by site and exercise in the 18-month-old equine distal metacarpal condyle. *Osteoarthritis and cartilage* **15**, 1283-1292 (2007).

44 Day, J. *et al.* Adaptation of subchondral bone in osteoarthritis. *Biorheology* **41**, 359-368 (2004).

45 Li, B. & Aspden, R. M. Mechanical and material properties of the subchondral bone plate from the femoral head of patients with osteoarthritis or osteoporosis. *Annals of the Rheumatic Diseases* **56**, 247-254 (1997).

46 Li, B. & Aspden, R. M. Composition and mechanical properties of cancellous bone from the femoral head of patients with osteoporosis or osteoarthritis. *Journal of Bone and Mineral Research* **12**, 641-651 (1997).

47 Jaiprakash, A. *et al.* Phenotypic characterization of osteoarthritic osteocytes from the sclerotic zones: a possible pathological role in subchondral bone sclerosis. *International journal of biological sciences* **8**, 406-417 (2012).

48 Couchourel, D. *et al.* Altered mineralization of human osteoarthritic osteoblasts is attributable to abnormal type I collagen production. *Arthritis & Rheumatism* **60**, 1438-1450 (2009).

49 Poulet, B. *et al.* Intermittent applied mechanical loading induces subchondral bone thickening that may be intensified locally by contiguous articular cartilage lesions. *Osteoarthritis and cartilage* **23**, 940-948 (2015).

50 Van Ruijven, L., Mulder, L. & Van Eijden, T. Variations in mineralization affect the stress and strain distributions in cortical and trabecular bone. *Journal of biomechanics* **40**, 1211-1218 (2007).

51 Mori, S., Harruff, R. & Burr, D. Microcracks in articular calcified cartilage of human femoral heads. *Archives of pathology & laboratory medicine* **117**, 196-198 (1993).

52 Pan, J. *et al.* Elevated cross-talk between subchondral bone and cartilage in osteoarthritic joints. *Bone* **51**, 212-217 (2012).

53 Suri, S. & Walsh, D. A. Osteochondral alterations in osteoarthritis. *Bone* **51**, 204-211 (2012).

54 Pouran, B. *et al.* Solute transport at the interface of cartilage and subchondral bone plate: effect of micro-architecture. *Journal of biomechanics* **52**, 148-154 (2017).

55 Muir, P. *et al.* Role of endochondral ossification of articular cartilage and functional adaptation of the subchondral plate in the development of fatigue microcracking of joints. *Bone* **38**, 342-349 (2006).

56 Laverty, S., Lacourt, M., Gao, C., Henderson, J. & Boyde, A. High density infill in cracks and protrusions from the articular calcified cartilage in osteoarthritis in standardbred horse carpal bones. *International journal of molecular sciences* **16**, 9600-9611 (2015).

57 Boyde, A. *et al.* On fragmenting, densely mineralised acellular protrusions into articular cartilage and their possible role in osteoarthritis. *Journal of anatomy* **225**, 436-446 (2014).

58 Turley, S. M., Thambyah, A., Riggs, C. M., Firth, E. C. & Broom, N. D. Microstructural changes in cartilage and bone related to repetitive overloading in an equine athlete model. *Journal of anatomy* **224**, 647-658 (2014).

59 Boyde, A. *et al.* Cartilage damage involving extrusion of mineralisable matrix from the articular calcified cartilage and subchondral bone. *Eur Cell Mater* **21**, 470-478 (2011).

60 Boyde, A. The real response of bone to exercise. *Journal of anatomy* **203**, 173-189 (2003).

61 Comhaire, F. H. & Snaps, F. Comparison of two canine registry databases on the prevalence of hip dysplasia by breed and the relationship of dysplasia with body weight and height. *American journal of veterinary research* **69**, 330-333 (2008).

62 Staines, K., Pollard, A., McGonnell, I., Farquharson, C. & Pitsillides, A. Cartilage to bone transitions in health and disease. *The Journal of endocrinology* **219**, R1-R12 (2013).

63 Staines, K. *et al.* Endochondral growth defect and deployment of transient chondrocyte behaviors underlie osteoarthritis onset in a natural murine model. *Arthritis & Rheumatology* **68**, 880-891 (2016).

64 Pitsillides, A. A. & Beier, F. Cartilage biology in osteoarthritis—lessons from developmental biology. *Nature Reviews Rheumatology* **7**, 654-663 (2011).

65 Puncreobutr, C., Lee, P., Hamilton, R. & Phillion, A. Quantitative 3D characterization of solidification structure and defect evolution in Al alloys. *Jom* **64**, 89-95 (2012).

66 Maksimcuka, J. *et al.* X-ray tomographic imaging of tensile deformation modes of electrospun biodegradable polyester fibers. *Frontiers in Materials* **4**, 43 (2017).

67 Poulet, B., Hamilton, R. W., Shefelbine, S. & Pitsillides, A. A. Characterizing a novel and adjustable noninvasive murine joint loading model. *Arthritis & Rheumatism* **63**, 137-147 (2011).

68 Nazarian, A., Stauber, M., Zurakowski, D., Snyder, B. D. & Müller, R. The interaction of microstructure and volume fraction in predicting failure in cancellous bone. *Bone* **39**, 1196-1202 (2006).

69 Rau, C., Wagner, U., Pešić, Z. & De Fanis, A. Coherent imaging at the Diamond beamline I13. *physica status solidi (a)* **208**, 2522-2525 (2011).

70 Pešić, Z., De Fanis, A., Wagner, U. & Rau, C. Experimental stations at I13 beamline at Diamond Light Source. *Journal of Physics: Conference Series* **425**, 182003 (2013).

71 Christen, D. *et al.* Deformable image registration and 3D strain mapping for the quantitative assessment of cortical bone microdamage. *Journal of the mechanical behavior of biomedical materials* **8**, 184-193 (2012).

72 Voide, R. *et al.* Time-lapsed assessment of microcrack initiation and propagation in murine cortical bone at submicrometer resolution. *Bone* **45**, 164-173 (2009).
73 Pacureanu, A., Langer, M., Boller, E., Tafforeau, P. & Peyrin, F. Nanoscale imaging of the bone cell network with synchrotron X-ray tomography: optimization of acquisition setup. *Medical physics* **39**, 2229-2238 (2012).
74 Basham, M. *et al.* Data analysis workbench (DAWN). *Journal of synchrotron radiation* **22**, 853-858 (2015).
75 Titarenko, V. Analytical formula for two-dimensional ring artefact suppression. *Journal of synchrotron radiation* **23**, 1447-1461 (2016).
76 Madi, K. *et al.* Computation of full-field displacements in a scaffold implant using digital volume correlation and finite element analysis. *Medical engineering & physics* **35**, 1298-1312 (2013).
77 Abd-Elmoniem, K. Z., Stuber, M. & Prince, J. L. Direct three-dimensional myocardial strain tensor quantification and tracking using zHARP. *Medical image analysis* **12**, 778-786 (2008).